Article

Effect of Pre-Weld Heat Treatment on the Microstructure and Properties of Coarse-Grained Heat-Affected Zone of a Wind Power Steel after Simulated Welding

Zhixing Wang, Xuelin Wang * and Chengjia Shang *

Collaborative Innovation Center of Steel Technology, University of Science and Technology Beijing, Beijing 100083, China; jason707165132@163.com
* Correspondence: xuelin2076@ustb.edu.cn (X.W.); cjshang@ustb.edu.cn (C.S.)

Abstract: The effect of pre-weld heat treatment on the microstructure and low-temperature impact toughness of the coarse-grained heat-affected zone (CGHAZ) after simulated welding was systematically investigated through the utilization of scanning electron microscopy (SEM) and electron back-scattering diffraction (EBSD). The Charpy impact test validated the presence of an optimal pre-weld heat treatment condition, resulting in the highest impact toughness observed in the CGHAZ. Three temperatures for pre-weld heat treatment (690, 720 and 750 °C) were used to obtain three different matrices (Steel 1, Steel 2, Steel 3) for simulated welding. The optimal pre-weld heat treatment is 720 °C for 15 min followed by water quench. Microstructure characterization showed that there is an evident microstructure comprising bainite (B) in Steel 1 and Steel 2 after pre-weld heat treatment, while the addition of martensite (M) with the pre-weld heat treatment temperature exceeds Ac_1 by almost 60 °C (Steel 3). These differences in microstructures obtained from pre-weld heat treatment influence the refinement of high-temperature austenite during subsequent simulated welding reheating processes, resulting in distinct microstructural characteristics in the CGHAZ. After the optimal pre-weld heat treatment, Steel 2 subjected to single-pass welding thermal simulation demonstrates a refined microstructure characterized by a high density of high-angle grain boundaries (HAGBs) within the CGHAZ, particularly evident in block boundaries. These boundaries effectively prevent the propagation of brittle cracks, thereby enhancing the impact toughness.

Keywords: wind power steel; simulated welding; pre-heat treatment; impact toughness; CGHAZ

1. Introduction

Wind power, as a renewable energy source, demonstrates substantial potential for future advancement. And in recent years, with the rapid development of wind power generation, in order to ensure the operational safety of wind power equipment (tubular steel tower), not only have the steel tube towers serving as supporting structures become increasingly larger, but also higher-strength advanced steel materials have been developed and utilized [1–3]. Research has revealed that TMCP steel plates exhibit superior service performance compared to conventionally processed steel plates in large wind turbine support structures [4–6]. Additionally, due to the fact that towers are predominantly constructed using methods of medium-thickness plate curling and welding, the key point of safety and stability throughout the operational lifespan of towers has shifted from the base material to the weld joint. And, it is widely acknowledged that the weld joint represents the region where materials are subjected to the welding thermal cycles, marked by rapid heating and variable cooling rates with high peak temperatures. These conditions have the potential to disrupt the optimal balance between high strength and toughness in the base material, which can disrupt the optimal balance of high strength and toughness in the base metal. Specifically, the coarse-grained heat-affected zone (CGHAZ) located within the weld joint consistently exhibits the worst toughness due to the formation of coarse

austenite grains and undesirable microstructure [7,8]. Previous studies have extensively investigated the influence of parameters such as alloy composition, welding heat input, cooling rate, post-weld heat treatment, etc., on the microstructure and properties of weld joints [9–12]. Moreover, studies have also found that pre-weld heat treatment can also affect the microstructure and mechanical properties of weld joints [13,14]. Furthermore, some studies have suggested that pre-weld heat treatment needs to be compatible with both the welding process and subsequent post-weld heat treatment to achieve favorable post-weld microstructure and mechanical properties [14,15]. From this, it can be seen that in addition to welding process parameters and alloy composition, the post-weld heat treatment for base materials and the degree of matching between post-weld heat treatment and welding process are also crucial.

Currently, the steels designed for wind power application with yield strengths of 500 MPa and a thickness of 25 mm are processed using the thermo-mechanical controlled process (TMCP); in special cases, pre-heating treatment is adopted. However, for this type of steel, research on the effect of pre-weld heat treatment on the microstructure and properties before and after welding remains insufficient. Therefore, this article prioritizes research on pre-weld heat treatment. Additionally, the optimal welding process for this novel thick-plate wind power steel was prioritized through simulated welding methods. By investigating the influence of different pre-weld heat treatment conditions on the microstructure of the CGHAZ after welding, as well as its low-temperature impact toughness, we provide theoretical and experimental bases for the development and application of wind power steel with high strength and good impact toughness. Furthermore, the microstructure visualization technique was employed to elucidate the correlation between the crystallographic structural entities and the paths of brittle crack propagation [16,17], such as blocks, and to elucidate the mechanisms impeding crack propagation.

2. Materials and Methods

In this study, the steels designed for wind power application with yield strengths of 500 MPa were used. This material features a thickness of 25 mm and was processed using the thermo-mechanical controlled process (TMCP). This composition adheres to a low-carbon plus micro-alloying philosophy, incorporating trace amounts of niobium (Nb) and titanium (Ti), consistent with a targeted alloy design system for enhanced material properties. The detailed chemical composition of the steel is presented in Table 1. The Ac_1 and Ac_3 temperatures of Q500 MPa grade wind power steel were calculated using JMatPro software (v12.1). As shown in Figure 1, the Ac_1 temperature was determined to be 693 °C, while the Ac_3 temperature was found to be 824 °C.
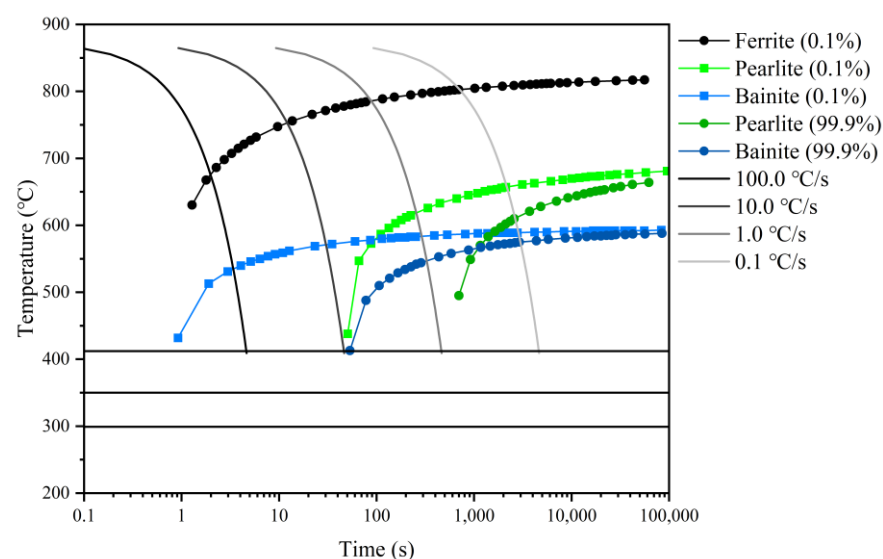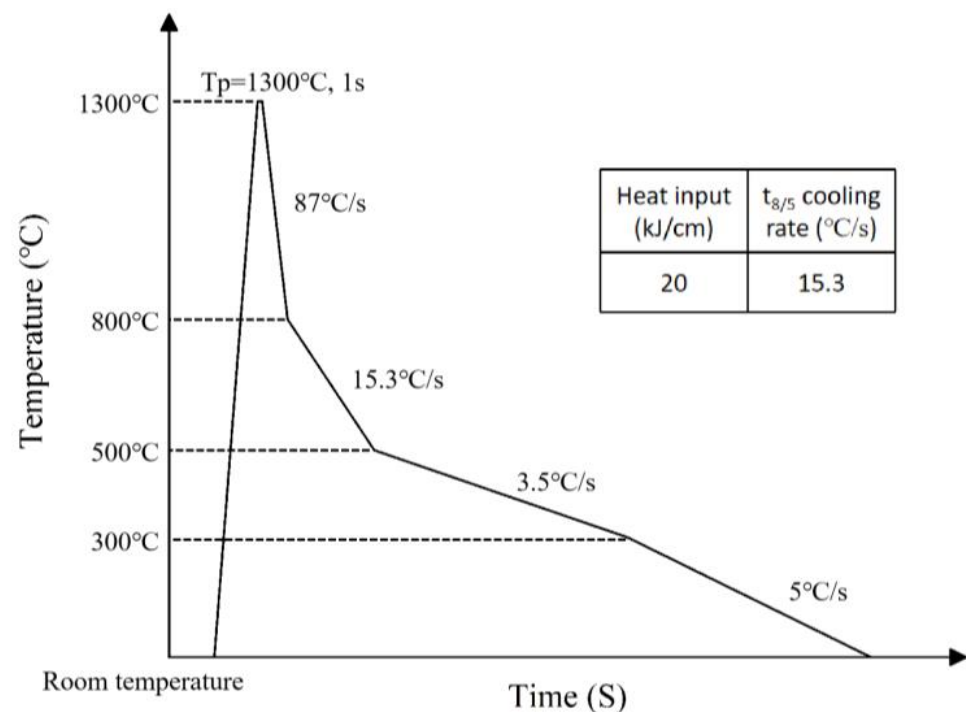

Figure 1. The CCT curve of the experimental steel.

Table 1. Chemical composition of the studied steel (wt. %).

C	Si	Mn	P	S	Cr + Ni + Nb + Ti
0.09	0.22	1.6	0.008	0.002	0.532

First, in order to investigate the influence of different pre-weld heat treatment conditions on the microstructure and impact toughness of CGHAZ, three proper temperatures below Ac_3 (690 °C, 720 °C, 750 °C) for quenching were chosen according to previous studies [18,19]. After 15 min in a vertical-type furnace, followed by water quenching, steels (Steel 1, Steel 2, Steel 3) with three different microstructures were obtained. After the heat treatments, welding simulation experiments (heat input: 20 kJ/cm) were conducted on three steels using a Gleeble-3500 (GTC, Dynamic Systems Inc., Poestenkill, NY, USA), with an average heating rate of 130 °C/s and a peak temperature of 1300 °C, to emulate the thermal cycling characteristic of CGHAZ during welding (Figure 2). The heating rate for simulated welding was determined according to the actual welding parameters employed for wind power steel, aligning with previous research [20].

Figure 2. Welding simulation process.

After welding simulation experiments, low-temperature toughness and hardness tests were conducted separately for the steel matrices and the thermal simulated samples. Hardness evolution from the CGHAZ to base material (BM) was measured using a 100 gf load and a dwell time of 15 s. And the hardness testing experiment was conducted under room-temperature conditions. Standard impact specimens with the size of 10 mm × 10 mm × 55 mm of both steel matrices (Steel 1, Steel 2, Steel 3) and thermal simulated samples were prepared to assess the Charpy V-Notch (CVN) impact toughness at the temperature of −60 °C.

Then, to observe the microstructures, the matrices and the regions subjected to welding simulation were, respectively, extracted from the steels that underwent pre-weld heat treatment and the welding-simulated samples. Scanning electron microscopy (SEM, TESCAN, Brno, Czech Republic) was utilized to observe the microstructures of the matrices, the welding simulation regions and the fracture surfaces obtained by Charpy impact tests. Among these samples, the matrices and welding simulation regions were mounted, mechanically polished and etched using 4% nital solution. The electron back-scattering diffraction (EBSD,

Oxford Instruments, Oxford, UK) analysis was conducted to both acquire crystallographic information regarding the transformation structure and investigate the correlation between crystallographic structure and crack propagation behavior in simulated CGHAZs, using TESCAN CLARA field emission SEM (TESCAN, Brno, Czech Republic) at an acceleration voltage of 20 kV, with a step size of 0.2 μm. All the samples for EBSD analysis underwent both mechanical and electrolytic polishing processes. To accomplish the visualization and digitization analysis of crystallographic features, both the HKL Channel 5 software and programs developed using MATLAB (version 2021, MathWorks, Natick, MA, USA) software were utilized. At the same time, by combining the above analysis and characterization approaches, the differences in impact toughness obtained from different samples were elucidated considering both microstructure transformation and crack propagation mechanisms.

3. Results and Discussion

3.1. Microstructure of the Matrix after Heat Treatment

Figure 3 shows the typical microstructure obtained from the matrix of the three steels (Steel 1, Steel 2 and Steel 3), corresponding to three different heat treatment temperatures (690 °C, 720 °C, 750 °C). Figure 3b, 3d and 3f are zoomed-in views of the regions in Figure 3a, 3c and 3e, respectively. It can be found that the matrix of Steel 1 and Steel 2 is composed of bainite (B), and the matrix of Steel 3 is mainly composed of typical bainite (B) with a small amount of martensite (M) and martensite/austenite (M/A) constituents. As Steel 1 is subjected to the heat treatment temperature of 690 °C, slightly below the Ac_1, followed by water quenching, it leads to the precipitation of coarse cementite, accompanied by the merging of bainitic laths (Figure 3a,b). Steel 2 undergoes the heat treatment process at a temperature of 720 °C, slightly above the Ac_1, also followed by water quenching. Due to the low degree of superheat, a minimal proportion of austenite is formed, resulting in a microstructure primarily consisting of bainite (B), with few martensites (M) observed. Additionally, with the heat treatment temperature of 720 °C, which is 30 °C higher than 690 °C, the diffusivity of carbon is enhanced, leading to the precipitation of a larger number of cementite particles with larger particle sizes (Figure 3c,d). In comparison to Steel 1 and 2, Steel 3 is subjected to the heat treatment temperature of 750 °C, surpassing the Ac_1 by approximately 60 °C. Consequently, an austenite reversion occurs, leading to the formation of reverted austenite. During the subsequent cooling process, the reverted austenite transforms into martensite (M), resulting in the microstructure of the Steel 3 matrix primarily consisting of bainite (B), and an amount of martensite and martensite/austenite (M/A) constituents (Figure 3e,f). In this work, the microstructural morphology of the matrix after intercritical heat treatment is consistent with previous studies [18,19,21–24].

3.2. Mechanical Properties and Impact Toughness of the Matrix after Heat Treatment

Figure 4 shows the low-temperature impact toughness and strength of the three steels (Steel 1, Steel 2 and Steel 3) and base material (BM), respectively. It is evident that the yield strength of Steel 1, Steel 2, Steel 3 and base material is 544, 520, 651 and 584 MPa, and the tensile strength of Steel 1, Steel 2, Steel 3 and base material is 640, 651, 864 and 667 MPa, respectively. Additionally, the difference in the elongation percentage among the three steels is minimal, with values of 13.4% (Steel 1), 15.5% (Steel 2), 14.6% (Steel 3) and 15.3% (base material), respectively. Notably, the matrix of Steel 3 exhibits higher yield strength and tensile strength compared to Steel 1, Steel 2 and base material, especially tensile strength. This is attributed to the fact that, after undergoing the heat treatment at 750 °C, the matrix structure of Steel 3 contains a certain amount of martensite, while the microstructures of Steel 1 and Steel 2 consist of bainite. This is also the reason why the elongation of Steel 3 is slightly lower than Steel 1, Steel 2 and base material (Figure 4). In addition, based on the impact toughness test results (Figure 4), it can be found that even if the test temperature is reduced to –60 °C, the low-temperature impact toughness of the three experimental steels can still exceed 300 J with 314.7 J (Steel 1), 321.7 J (Steel 2) and 301.1 J (Steel 3), respectively. Furthermore, the differences in impact toughness among the

matrix of three steels are not significant, the presence of martensite in the microstructure of Steel 3 contributes to the slightly lower impact toughness. However, the low-temperature impact toughness of the base material is relatively low. This indicates that the matrix of experimental steels after heat treatment has excellent comprehensive properties.
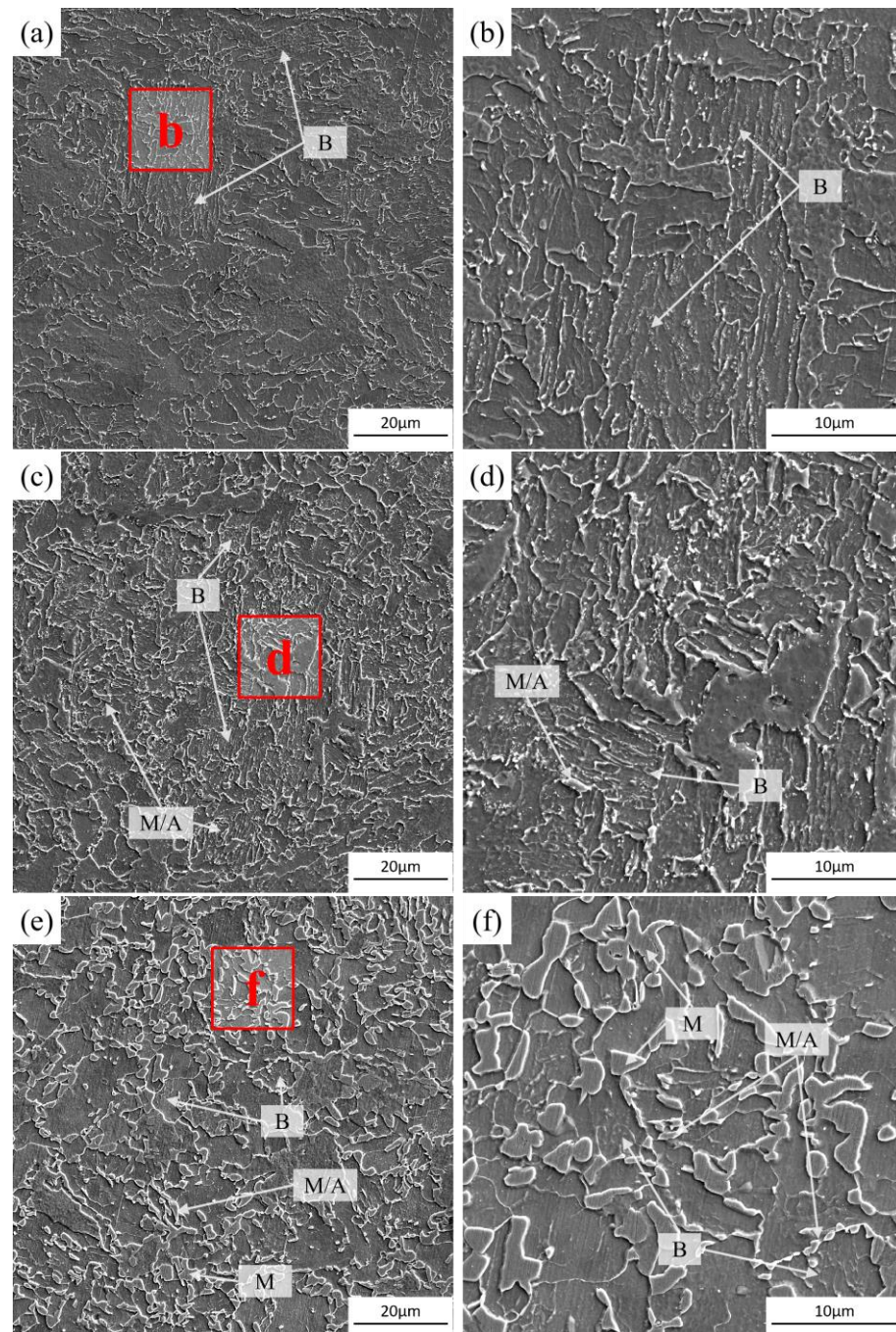

Figure 3. SEM images showing the microstructure of the matrix of Steel 1 (**a,b**), Steel 2 (**c,d**) and Steel 3 (**e,f**).

3.3. Impact Toughness of the Simulated CGHAZ

Figure 5 displays the impact toughness of simulated CGHAZs with the same heat input (20 kJ/cm) using the three steels (BM, base metal) subjected to three different pre-weld heat treatment processes as a welding matrix. It is evident that the impact toughness of Steel 2 is the highest of the three and reaches 241.1 J. In comparison, the impact toughness

of the CGHAZ decreased by 41% for Steel 1 (141.7 J) and 67% for Steel 3 (79.7 J), respectively. It indicates that there is an optimum pre-weld heat treatment condition before the welding of the steel in this study. With the higher or lower pre-weld heat treatment temperatures, the low-temperature impact toughness of the CGHAZs will be affected, significantly. These results are further supported by the examination of impact fracture morphology, as shown in Figure 6. Additionally, after undergoing three different heat treatment processes, the impact toughness of the matrices of Steel 1, Steel 2 and Steel 3 have relatively small errors, but the errors in the simulated CGHAZs are larger. This is because the different regions of the simulated welding samples undergo varying thermal cycles, resulting in significant differences in the microstructure of the simulated weld heat-affected zone (HAZ), including the CGHAZ, fine-grained heat-affected zone (FGHAZ) and so on. This complex microstructural composition can lead to potential errors in impact toughness.
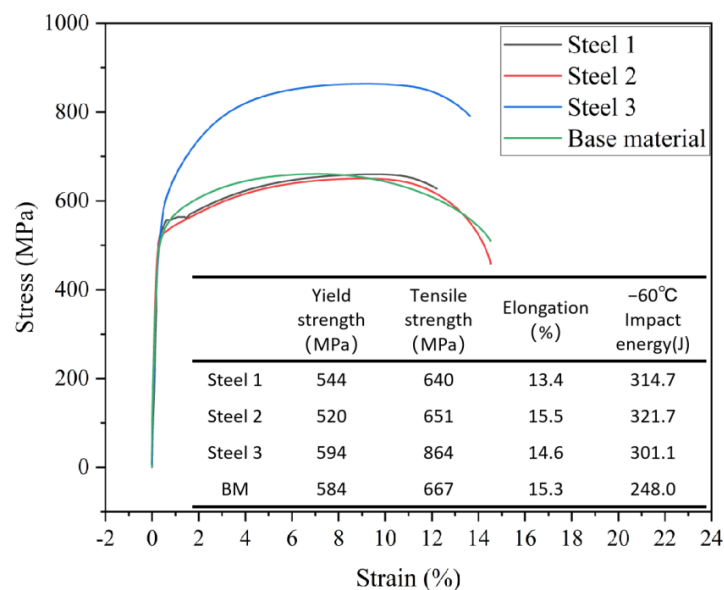

	Yield strength (MPa)	Tensile strength (MPa)	Elongation (%)	−60°C Impact energy(J)
Steel 1	544	640	13.4	314.7
Steel 2	520	651	15.5	321.7
Steel 3	594	864	14.6	301.1
BM	584	667	15.3	248.0

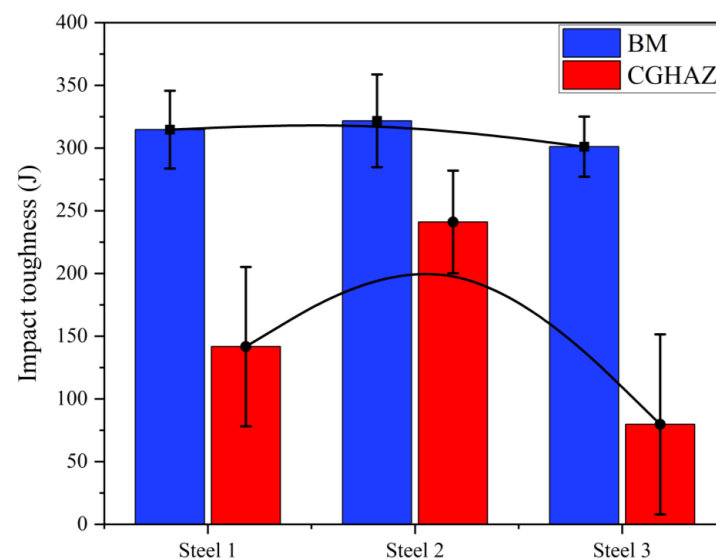**Figure 4.** Stress–strain curves of three steels and base material.

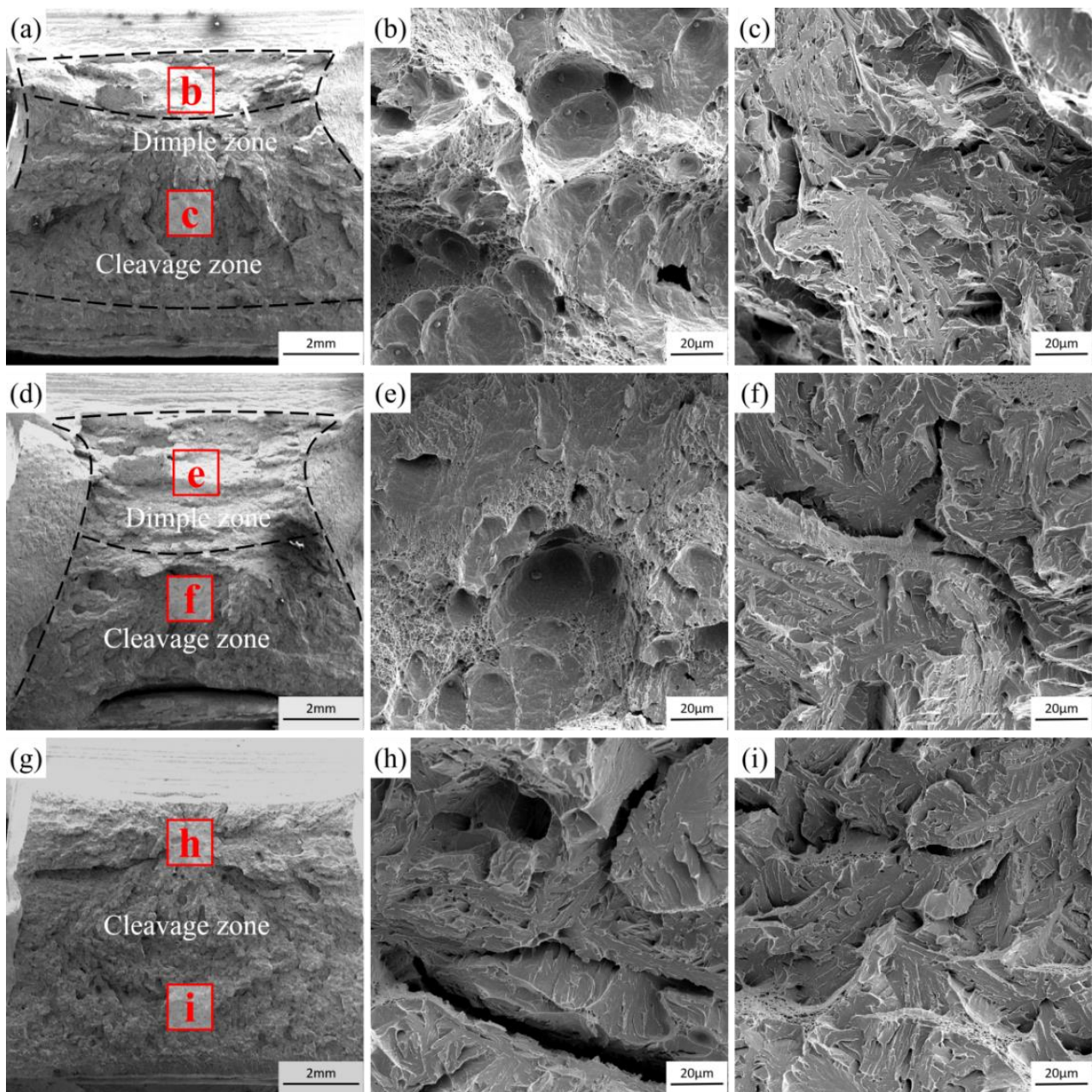**Figure 5.** Low-temperature impact toughness of BM and CGHAZ of three steels.

Figure 6. SEM fracture surface micrographs of the welding simulated samples under the heat input: 20 kJ/cm. (**a**–**c**) Steel 1, (**d**–**f**) Steel 2 and (**g**–**i**) Steel 3.

Figure 6 shows the SEM morphology of the impact fracture. Figure 6a, 6d and 6g represent the overall morphology of impact fracture of Steel 1, Steel 2 and Steel 3, respectively. As shown in the zoomed-in views of Steel 1 and Steel 2, the fracture surface of the CGHAZs exhibits both ductile and brittle fracture characteristics, with the dimple (Figure 6b,e) and cleavage (Figure 6c,f) patterns distributed. By contrast, the fracture surface of the CGHAZ (Steel 3), the complete cleavage fracture morphology is presented (Figure 6g,h,i), indicating the lowest low-temperature impact toughness. It can also be observed that the area fraction of dimple fracture morphology in the CGHAZ of Steel 2 (Figure 6d) is larger than that of Steel 1 (Figure 6a), which is in line with the trend of low-temperature impact toughness variation. Moreover, the dimple fracture morphology is characterized by numerous small-sized dimples and a lesser number of large shallow ones. Some large dimples are accompanied by smaller ones, resulting in an inconsistent dimple size distribution (Figure 6b,e). During impact testing, dimples demonstrate strong

energy absorption capabilities. Hence, the CGHAZ of Steel 2 exhibits relatively higher impact toughness.

Previous studies have shown that the microstructural transformations during the welding process influence the microstructure of the HAZ, especially within the CGHAZ, consequently affecting its low-temperature impact toughness [25–27]. In this study, the low-temperature impact toughness obtained in the CGHAZs of Steel 1, 2 and 3 are quite different, which should be influenced by the difference in microstructures. Since the experimental steels used in this study have identical compositions and the simulated welding processes are also identical, the differences in the microstructural characteristics within these CGHAZs are inevitably attributed to the differences in the microstructures of the matrix for welding resulting from different heat treatment conditions before simulated welding. In addition, the low-temperature impact toughness is not only determined by the phase transformation but is also related to the grain boundary density. These will be discussed in detail in the following paragraphs.

3.4. Hardness of the Simulated CGHAZ

Figure 7 depicts the hardness distribution across different regions of three steel plates after simulated welding, showing minimal overall differences among the three samples. Notably, although Steel 1, Steel 2 and Steel 3 exhibit different matrix microstructures, their hardness differences are minimal, lower than 7 HV. The average hardness value of the BM (Steel 1) reaches 201 HV due to its matrix microstructure being composed of lath bainite (LB). Meanwhile, due to the increase in lath bainite (LB) in Steel 2, the spacing between laths is smaller than in Steel 1, resulting in a slight increase in the average hardness value to 207 HV. Additionally, although the content of lath bainite (LB) decreased in the matrix of Steel 3, the presence of martensite ensures that its average hardness value still reaches 200 HV. The hardness values of the CGHAZ are approximately the same, with hardness values fluctuating within a range from 280 HV (CGHAZ of Steel 3) to 290 HV (CGHAZ of Steel 1). This consistency is attributed to the existence of lath bainite (LB) within the CGHAZ.
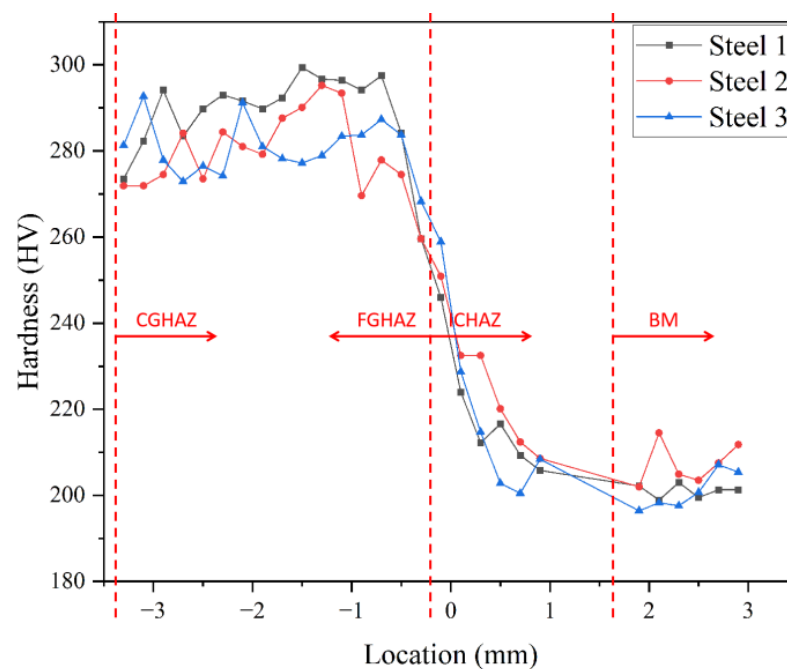

Figure 7. Hardness testing result of simulated samples from CGHAZ to BM.

3.5. Microstructure of the Simulated CGHAZ

Many studies have indicated that the microstructure of the welded CGHAZ influences its impact toughness [27–29]. Furthermore, under the same welding thermal simulation

process, the prior austenite grain (PAG) affects the microstructural characteristics within the CGHAZ after cooling during the welding process. The morphology and sizes of PAGs in the CGHAZ of Steel 1, 2 and 3 were measured by analyzing and processing the EBSD images using AZtecCrystal software (v2.2). As shown in Figure 8, the grain boundaries of the prior austenite grain within the CGHAZ of the three steels are prominently visible, with relatively large grain sizes. Among them, after the simulated welding, the CGHAZ of Steel 3 exhibits the largest size of prior austenite grain (PAG) (Figure 8c), with an equivalent circular diameter of approximately 78 μm, while the CGHAZ of Steel 2 exhibits the smallest PAG size (Figure 8b), with an equivalent circular diameter of approximately 62 μm.
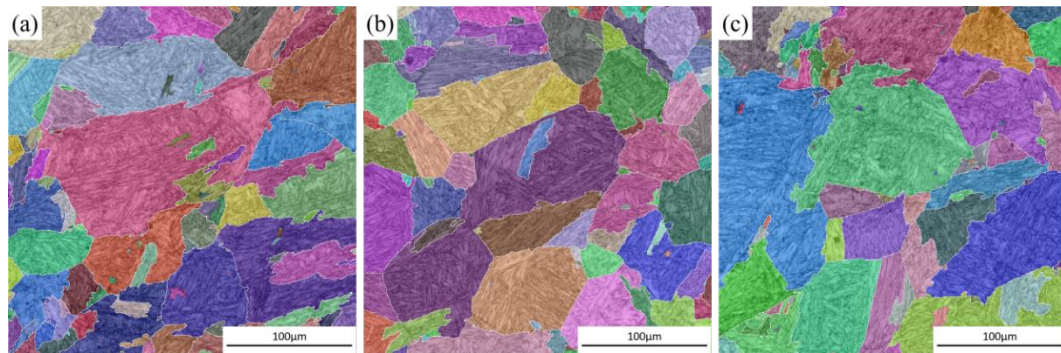

Figure 8. Reconstruction of austenite in CGHAZ of Steel 1 (**a**), Steel 2 (**b**) and Steel 3 (**c**).

The differences in the size of the prior austenite grains in CGHAZs are attributed to the variations in the microstructural characteristics of the welding matrix, which result from different heat treatment processes before simulated welding. Previous studies clarify that the initial microstructure significantly influences the austenite reversion even when the alloy and temperature are consistent [30]. As shown in Figure 3e,f, Steel 3 as the welding matrix consists of martensite (M), resulting in the formation of acicular austenite during the austenite reversion. Generally, acicular austenite exhibits the same orientation as the prior austenite grains, leading to the memory effect which does not facilitate the refinement of austenite grains during the welding process [21,31–34]. This is the primary reason for the CGHAZ of Steel 3 exhibiting the largest PAG size (Figure 8c). In the austenite reversion from martensite, two typical morphologies of austenite were widely observed, which are fine acicular and coarse globular austenite [35–37]. Specifically, at high degrees of superheat, acicular austenite forms near the Ac_1. As the temperature increases, thin acicular austenite grains grow along the lath or block boundaries and hold a near Kurdjumov–Sachs (K-S) orientation relationship (OR) with its neighboring martensite matrix, restoring the prior austenite grain shape and size, resulting in the inheritance of the coarse prior austenite grain. Nevertheless, the prior austenite grains within the CGHAZs of Steel 1 and 2 are smaller than the ones of Steel 3. And this difference is also attributed to the difference in the microstructure of the welding matrix. As shown in Figure 3, there is a coarse cementite particle distribution in the matrix of Steel 1 and Steel 2, which is conducive to the nucleation of reverted austenite, subsequently leading to the refinement of austenite grains. It was reported that pre-tempering [36] or slower heating rates [37] influence the cementite (θ) particle distribution and composition, and cementite (θ) particles play key roles in the austenite reversion. Theoretical analysis indicates that the coarser cementite particles have a higher potency for austenite nucleation [30], and thus the coarsening of the cementite particles obtained by pre-weld heat treatment at 690 °C and 720 °C in this work promotes its formation during the simulated welding process, leading to the refinement of austenite grains. Furthermore, the cementite particles in the matrix of Steel 2 are not only larger than those in Steel 1 but also have a greater quantity, resulting in the differences in the size of the prior austenite grains in CGHAZs between Steel 1 (Figure 8a) and Steel 2 (Figure 8b).

The differences in the size of the prior austenite grains can result in differences in the microstructure of the CGHAZs, thereby affecting the impact toughness (−60 °C) of

CGHAZs. After simulated welding experiments, as shown in Figure 9, the microstructures in the CGHAZs of the three steels are predominantly composed of lath bainite (LB). In the CGHAZ of Steel 1 (Figure 9a) and Steel 3 (Figure 9c), the bainitic lath is longer, almost running through the entire austenite grain, whereas in Steel 2 (Figure 9b), the bainitic lath is shorter, forming a greater number of microstructures with different orientations.
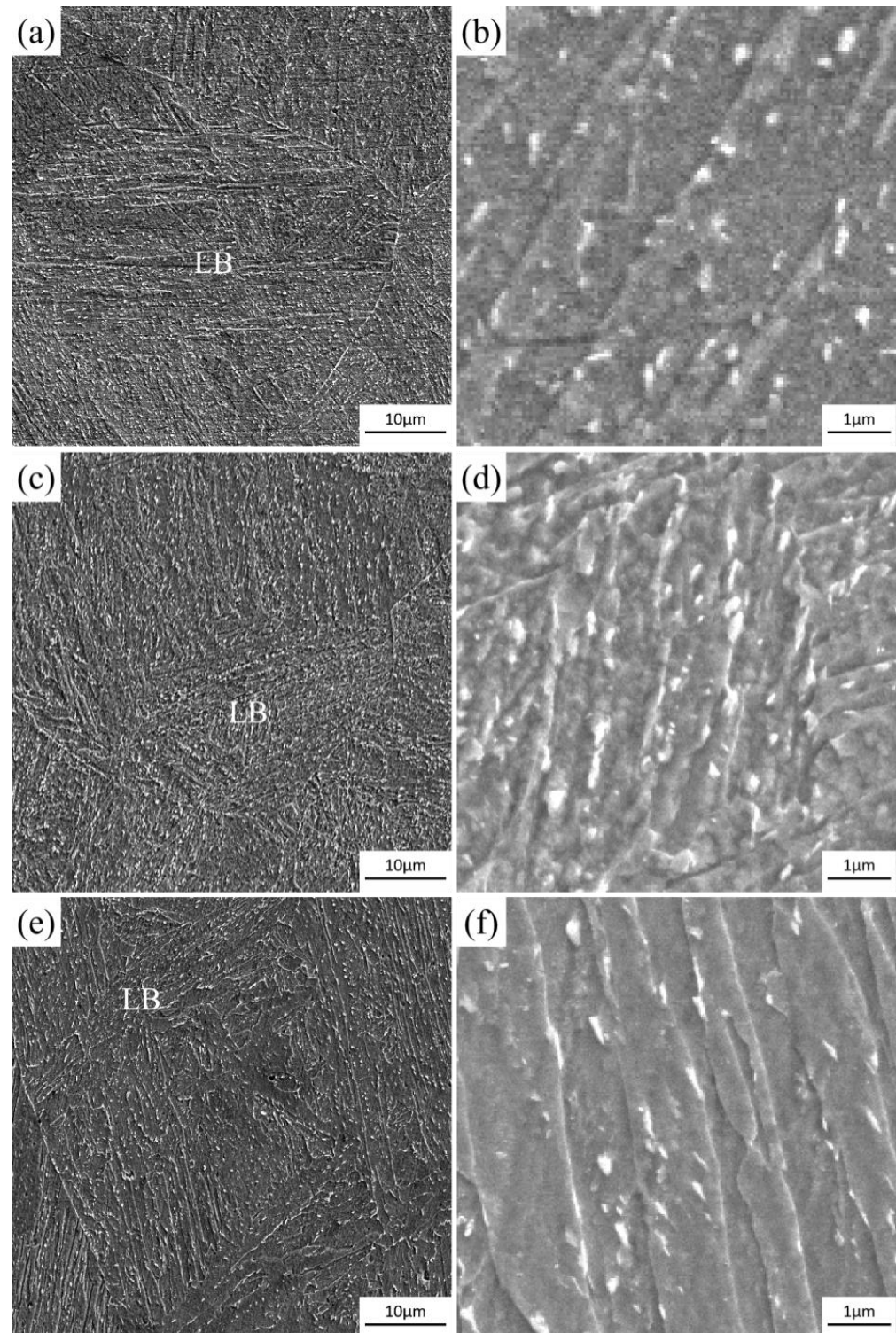

Figure 9. SEM images of microstructure in simulated CGHAZs: (**a,b**) Steel 1, (**c,d**) Steel 2 and (**e,f**) Steel 3.

The size of prior austenite grains exerts a certain influence on the nucleation and growth of bainite. Bainite nucleation primarily occurs at the prior austenite grain boundaries, followed by growth within the grains. And, the effective nucleation area of the grain boundaries per unit volume, denoted as S_{vo} (mm^{-1}), can be mathematically expressed as Equation (1) [38].

$$S_{vo} = 2000/d_\gamma \tag{1}$$

where d_γ represents the size of austenite grains. In this study, when the size of the prior austenite grains decreases from 78 μm in Steel 3 to 62 μm in Steel 2, the parameter S_{vo} increases from 25.6 mm^{-1} to 32.3 mm^{-1}. The smaller-sized prior austenite grains provide a higher density of effective grain boundaries for the nucleation of bainite in the matrix [39]. Within a coarse austenite grain, the bainite transformation exhibits a distinctive two-stage nucleation behavior. The first stage involves primary laths nucleating at the boundaries and growing toward the interior of the austenite grain. The subsequent stage comprises the nucleation of secondary laths, which attach to the primary laths and grow in the other direction. Additionally, in the absence of influence from other bainitic laths, bainitic laths will grow to the grain boundary, forming bainitic laths that traverse the entire grain. Otherwise, they will form shorter bainitic laths with different orientations [39]. Therefore, there is a certain relationship between the length of bainitic laths and the size of austenite grains, which increases with the increasing size of austenite grains [40].

3.6. Crystallographic Structure and Grain Boundary Analysis of the Simulated CGHAZ

To further elucidate the influence of different sizes of prior austenite grains on the microstructure and low-temperature impact toughness of CGHAZs, Figure 10 displays the inverse pole figures (IPF) and the maps of grain boundary distribution. Different colored lines are used to outline the grain boundaries with different orientations, where the white line denotes the interface with orientations ranging from 5 to 15 degrees, the black line is the interfaces with orientations ranging from 15 to 45 degrees, and the yellow line is the interfaces with orientations of more than 45°. Comparing the IPF and grain boundary distribution diagrams, it can be found that with the change in the size of the prior austenite grains affected by the changes in the microstructural characteristics of the welding matrix, the morphology and grain boundary distribution appear to change greatly. The CGHAZ of Steel 2 obtained from simulated welding has a higher density of high-angle grain boundaries (HAGBs) and finer microstructures than those of Steel 1 and Steel 3. On the contrary, if the size of the prior austenite grains increases, the density of HAGBs decreases, especially in the CGHAZ of Steel 3 (Figure 10f), indicating a significant coarsening of the effective grain size consisting of many low-angle grain boundaries (LAGBs). Previous research has indicated that the misorientation of the high-angle boundaries has the capability to arrest brittle cracks. Specifically, those interfaces exceed 45 degrees, which consistently exhibits specific misorientations within the corresponding prior austenite grain [41]. And this series of crystallographic structural evolution is principally governed by the bainite variant selection.
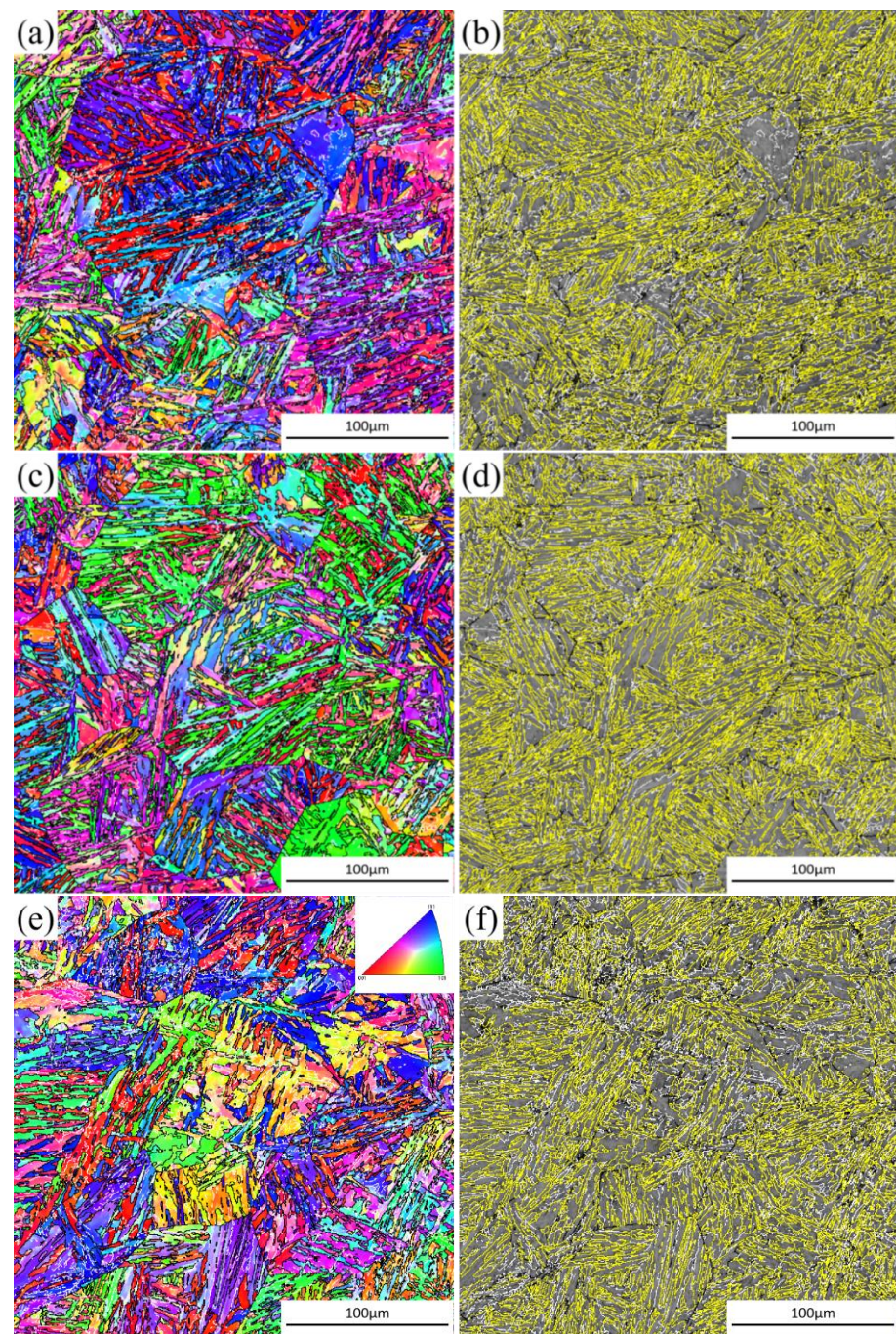
Figure 10. Inverse pole figures and boundary distributions of the simulated samples under the heat input: 20 kJ/cm. (**a**,**b**) CGHAZ of Steel 1, (**c**,**d**) CGHAZ of Steel 2 and (**e**,**f**) CGHAZ of Steel 3.

Moreover, research indicates that the variant selection within refined austenite grains significantly contributes to the increase in high-angle grain boundary (HAGB) density [42]. For the 500 MPa wind power steel investigated in this study, the lath microstructure characteristics indicate that the internal structure of each prior austenite grain should satisfy or approximately satisfy the characteristics of the coherent phase transformation. Therefore, there exist packet boundaries, block boundaries and sub-block boundaries [43]. As illustrated in Figure 11, the boundary densities in the CGHAZ of three steels were calculated. Overall, in the CGHAZ of Steel 2, the high-angle grain boundary (HAGB) length is the longest, and the low-temperature impact toughness of the CGHAZ is the highest (Figure 11b,d). Significantly, the density of the block boundaries in the CGHAZ

of Steel 2 is also the highest due to the most refined prior austenite grains obtained in this study (Figure 8b). And, with the increasing size of the prior austenite grains, the density of the block boundaries in the CGHAZs decreases.
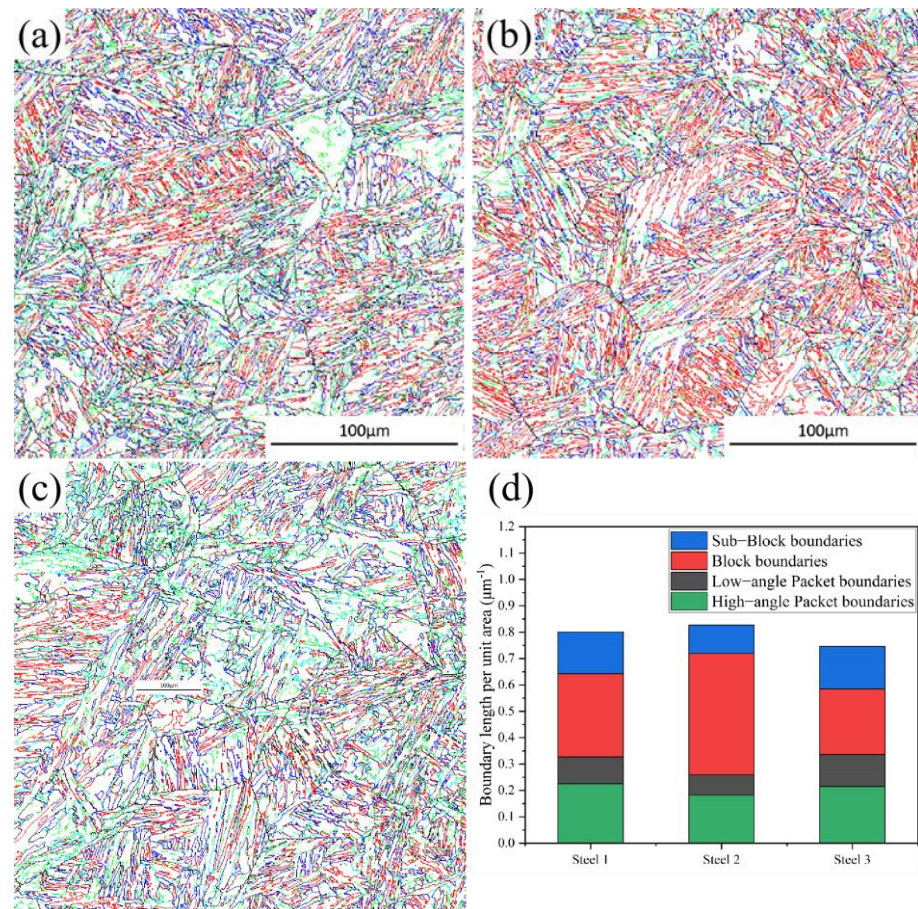

Figure 11. Boundary density in the CGHAZ of the simulated samples at the heat input of 20 kJ/cm: (**a**) Steel 1, (**b**) Steel 2, (**c**) Steel 3 and (**d**) boundary density. Black line: PAG boundaries; Red line: Block boundaries; Green line: Sub-Block boundaries; Blue line: High-angle Packet boundaries; Cyan line: Low-angle Packet boundaries.

3.7. Correlation between Crystallographic Structure and Brittle Crack Propagation Path

Figure 12 shows the secondary cracks that emerge on the fracture surface governed by the LB structures in the CGHAZ of Steel 1 (Figure 12a,d,g), Steel 2 (Figure 12b,e,h) and Steel 3 (Figure 12c,f,i). With the increasing size of the austenite grain, the bainite transformation structure exhibits a greater tendency to form block or packet units characterized by a parallel arrangement, consequently resulting in a notable increase in the likelihood of brittle crack propagation parallel to the block during the impact test, leading to a decrease in the absorption energy of crack propagation. This ultimately reflects that, despite all three samples having LB structure, the propagation path differs due to variations in structural arrangement in crystallography. The crack paths in the CGHAZ of Steel 1 (Figure 12a) and Steel 3 (Figure 12c) are relatively straightforward, while the crack path in the CGHAZ of Steel 2 (Figure 12b) is more tortuous. This is because of the difference in the density of block boundaries in the CGHAZ. The block boundaries significantly increased the density of HAGBs, thereby effectively hindering brittle crack propagation at the boundaries of Bain zones and inducing a tortuous propagation path.
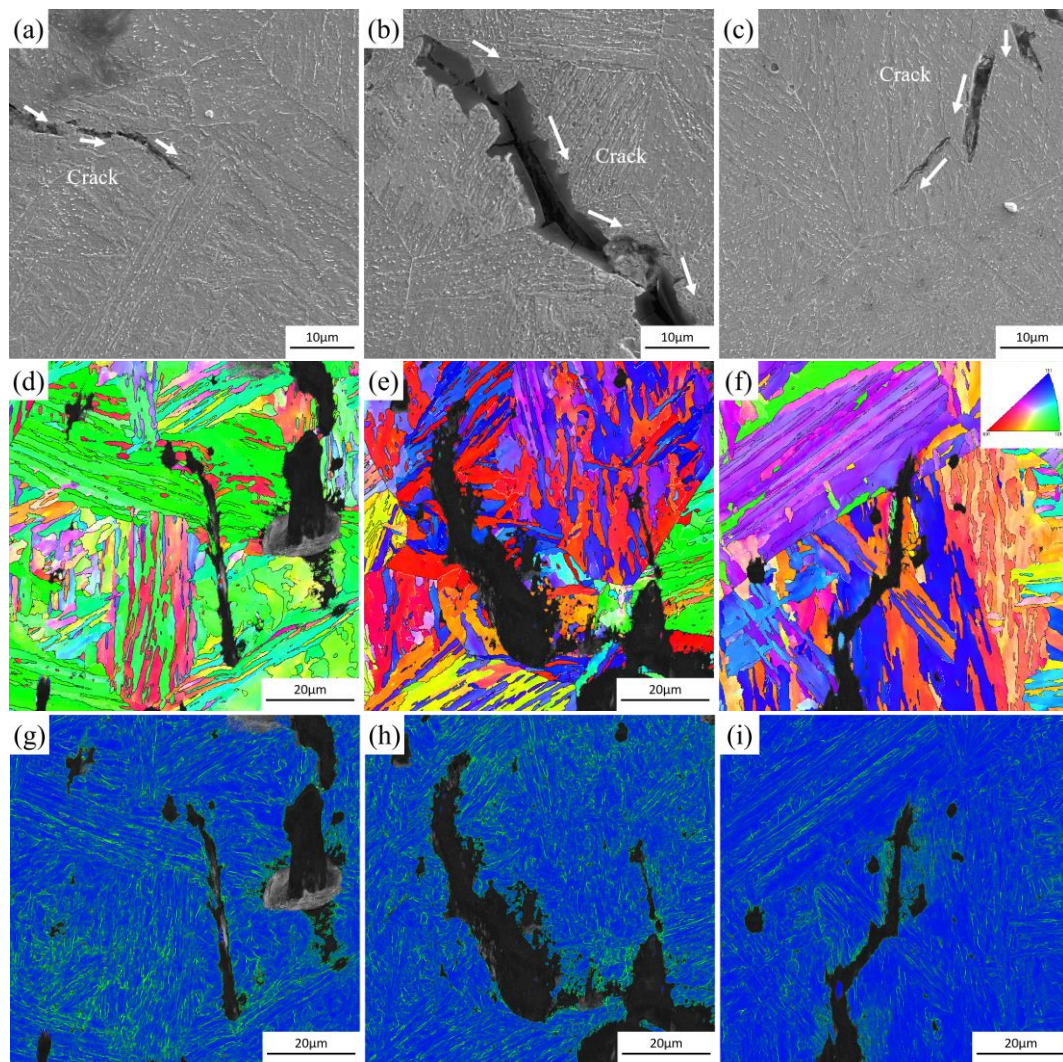
Figure 12. Morphology of secondary cracks by SEM: (**a**,**d**,**g**) Steel 1, (**b**,**e**,**h**) Steel 2 and (**c**,**f**,**i**) Steel 3.

A previous study found that the presence of high grain boundary misorientation does not necessarily guarantee a high angular deviation in cleavage crack propagation, not all of the prior austenite grain boundaries (PAGBs) are effective in impeding crack propagation [44]. In certain cases, the cleavage crack propagation may occur across the adjacent grains without exhibiting any angular deviation, even though their interface is a prior austenite grain boundary (PAGB), which belongs to HAGBs. However, due to their significantly higher density compared to PAGBs, the boundaries within austenite grains play a leading role in crack propagation. Additionally, previous studies have also indicated that the size of the austenite grain and the proportion of microstructure also affect the impact toughness [45,46]. Therefore, in this study, the impact on crack propagation cannot be discussed solely by using PAGBs or the boundaries inside the austenite grain, and both must be combined for analysis.

From Figure 12i, it is also evident that there is minimal plastic deformation surrounding the propagation path of these secondary cracks, indicating that the fracture facet corresponding to the crack is primarily a cleavage fracture rather than a dimple. Nevertheless, the crack was ultimately arrested at the PAGB (Figure 12f). By contrast, from Figure 12h, there exists notable plastic deformation along the propagation path of secondary cracks, suggesting that the fracture facet associated with the crack is dimple fracture rather than cleavage. In addition, this crack was eventually arrested inside the grain instead of at the PAGBs (Figure 12e). Additionally, secondary cracks in the CGHAZ of Steel 1 and

Steel 3 deviated three times each, while cracks in the CGHAZ of Steel 2 deviated four times. This is attributed to the lower density of HAGBs in Steel 1 and 3, whereas relatively, Steel 2 contains a higher density of HAGBs, including prior PAGBs. Due to the excellent performance of HAGBs in hindering crack propagation, they can absorb the energy during crack extension. Therefore, when cracks propagate to HAGBs, a significant reduction in internal energy occurs, effectively inhibiting further crack propagation. Furthermore, the LB structure exhibits an interactive arrangement in the CGHAZ of Steel 2, which promotes the continuous deflection of brittle crack propagation, thereby enhancing the propagation resistance and increasing the impact absorption energy. This is close to the outcomes of the impact test (Figure 5). The presence of large cleavage facets on the fracture surface of both Steel 1 and 3 can be attributed to their coarse microstructures characterized by a low density of HAGBs. Conversely, the reduced size of cleavage facets observed in Steel 2 can be attributed to the microstructural refinement within the CGHAZ.

In summary, the difference in microstructural proportions does affect the low-temperature impact toughness, particularly in the case of actual welded joints. This study focuses on improving the welding matrix through heat treatment processes, which consequently leads to the improvement of microstructures within the CGHAZ, aiming to enhance the impact toughness of welded joints. Understanding the impact of the welding matrix on the post-weld microstructure and the mechanisms through which various microstructures affect both crack propagation and low-temperature impact toughness is helpful in guiding actual welding engineering. Therefore, for achieving excellent comprehensive properties in both base material and welding HAZ concurrently, it is essential to appropriately match the pre-welding heat treatment with the welding process. Currently, for the new 500 MPa-grade high-strength wind power steel, under the condition of a heat input of 20 kJ/cm, favorable low-temperature impact toughness can be achieved. The strength and toughness of both the matrix and HAZ are excellent, demonstrating good overall performance. Additionally, the actual welding experiments on samples subjected to pre-weld heat treatment are currently in progress, and the research results on the microstructure and properties of actual welded samples will be published gradually in the future.

4. Conclusions

1. The optimal pre-weld heat treatment process suitable for 500 MPa-grade wind power steel was determined. The results of simulated welding experiments also demonstrate that the welding process with a heat input of 20 kJ/cm, matched well with the pre-weld heat treatment process in this study, resulting in excellent overall mechanical properties and low-temperature toughness before and after welding. This study provides experimental data support for subsequent actual welding experiments and engineering applications, which is of guiding significance.
2. The wind power steel, with a strength grade of 500 MPa, processed by the TMCP method, demonstrates an optimum heat treatment before welding (720 °C for 15 min followed by water quenching). After pre-weld heat treatment, the yield strength of the steel matrix also meets the requirement of 500 MPa. The yield strength reaches 520 MPa, the tensile strength reaches 651 MPa, and the impact toughness at −60 °C reaches 321.7 J. Additionally, it also ensures the excellent impact toughness of the post-weld CGHAZ.
3. The microstructure of the welding matrix significantly influences the microstructure and properties of the post-weld CGHAZ. After pre-weld heat treatment at 720 °C, the post-weld microstructure can achieve the best impact toughness, while at 750 °C and 690 °C, the impact toughness is relatively lower, especially at 750 °C. This is attributed to the formation of martensite in the matrix obtained from the 750 °C pre-weld heat treatment, which leads to the coarsening of austenite during the welding process.
4. The microstructure of the welding matrix after the pre-weld heat treatment at 720 °C consists of bainite (B) and acicular ferrite (AF), with a certain amount of cementite particles. These microstructural characteristics are helpful in controlling the refine-

ment of austenite grains during the welding process. Therefore, using steel plates treated at 720 °C as the welding matrix results in a microstructure of CGHAZ dominated by lath bainite, with a high density of high-angle grain boundaries (HAGBs). These boundaries effectively prevent the propagation of brittle cracks, especially the block boundaries.

Author Contributions: Conceptualization, Z.W. (Zhixing Wang), X.W. (Xuelin Wang) and C.S. (Chengjia Shang); methodology, Z.W. (Zhixing Wang) and X.W. (Xuelin Wang); software, Z.W. (Zhixing Wang); validation, Z.W. (Zhixing Wang) and X.W. (Xuelin Wang); formal analysis, Z.W. (Zhixing Wang) and X.W. (Xuelin Wang); investigation, Z.W. (Zhixing Wang) and X.W. (Xuelin Wang); resources, X.W. (Xuelin Wang) and C.S. (Chengjia Shang); data curation, Z.W. (Zhixing Wang); writing—original draft preparation, Z.W. (Zhixing Wang); writing—review and editing, Z.W. (Zhixing Wang), X.W. (Xuelin Wang) and C.S. (Chengjia Shang); visualization, Z.W. (Zhixing Wang); supervision, X.W. (Xuelin Wang) and C.S. (Chengjia Shang); project administration, X.W. (Xuelin Wang) and C.S. (Chengjia Shang); funding acquisition, X.W. (Xuelin Wang) and C.S. (Chengjia Shang). All authors have read and agreed to the published version of the manuscript.

Data Availability Statement: The original contributions presented in the study are included in the article, further inquiries can be directed to the corresponding author.

Conflicts of Interest: The authors declare no conflicts of interest.

References

1. Wang, B.; Wang, J.; Guan, Y.; Ren, L.; Ning, K.; Zhang, W. Study on the safety performance of large offshore wind turbine coupling. *Ocean. Eng.* **2023**, *279*, 114525. [CrossRef]
2. Zheng, D.; Guo, H.; Zhang, S.; Liu, Y. Study on fatigue performance of double cover plate through-core bolted joint of rectangular concrete-filled steel tube bundle wind turbine towers. *J. Constr. Steel Res.* **2023**, *203*, 107830. [CrossRef]
3. Niklas, K.; Bera, A.; Garbatov, Y. Impact of steel grade on a ship colliding with an offshore wind turbine monopile supporting structure. *Ocean Eng.* **2023**, *287*, 115899. [CrossRef]
4. Igwemezie, V.; Mehmanparast, A.; Kolios, A. Materials selection for XL wind turbine support structures: A corrosion-fatigue perspective. *Mar. Struct.* **2018**, *61*, 381–397. [CrossRef]
5. Igwemezie, V.; Dirisu, P.; Mehmanparast, A. Critical assessment of the fatigue crack growth rate sensitivity to material microstructure in ferrite-pearlite steels in air and marine environment. *Mater. Sci. Eng. A* **2019**, *754*, 750–765. [CrossRef]
6. Igwemezie, V.; Mehmanparast, A.; Kolios, A. Current trend in offshore wind energy sector and material requirements for fatigue resistance improvement in large wind turbine support structures–A review. *Renew. Sustain. Energy Rev.* **2019**, *101*, 181–196. [CrossRef]
7. Shao, J.; Fei, J.; Zhong, S.; Zhao, L.; Xu, L.; Han, Y. Microstructure and properties of intercritically reheated coarse-grained heat affected zone in X65 pipeline steel with pre-strain. *Int. J. Hydrog. Energy* **2024**, *49*, 1345–1357. [CrossRef]
8. Lan, L.; Qiu, C.; Zhao, D.; Gao, X.; Du, L. Microstructural characteristics and toughness of the simulated coarse grained heat affected zone of high strength low carbon bainitic steel. *Mater. Sci. Eng. A* **2011**, *529*, 192–200. [CrossRef]
9. Bertolo, V.; Jiang, Q.; Sanchez, M.T.; Riemslag, T.; Walters, C.; Sietsma, J. Cleavage fracture micromechanisms in simulated heat affected zones of S690 high strength steels. *Mater. Sci. Eng. A* **2023**, *868*, 144762. [CrossRef]
10. Yang, Y.; Jia, X.; Ma, Y.; Wang, P.; Zhu, F. Effect of Nb on inclusions and phase transformation in simulated high heat input coarse-grain HAZ of Nb/Ti low carbon microalloyed steel. *Mater. Charact.* **2022**, *189*, 111966. [CrossRef]
11. Sisodia, R.; Weglowski, M.; Sliwinski, P. In situ localised post-weld heat treatment with electron beam welding of S690QL steel. *J. Adv. Join. Process.* **2024**, *9*, 100182. [CrossRef]
12. Shi, Y.; Chen, D.; Lei, Y.; Li, X. HAZ microstructure simulation in welding of a ultra fine grain steel. *Comput. Mater. Sci.* **2004**, *31*, 379–388. [CrossRef]
13. Kuryntsev, S.V. The influence of pre-heat treatment on laser welding of T-joints of workpieces made of selective laser melting steel and cold rolled stainless steel. *Opt. Laser Technol.* **2018**, *107*, 59–66. [CrossRef]
14. Panov, D.; Naumov, S.; Stepanov, N.; Sokolovsky, V. Effect of pre-heating and post-weld heat treatment on structure and mechanical properties of laser beam-welded Ti2AlNb-based joints. *Intermetallics* **2022**, *143*, 107466. [CrossRef]
15. Avettand-Fènoël, M.N.; Taillard, R. Effect of a pre or postweld heat treatment on microstructure and mechanical properties of an AA2050 weld obtained by SSFSW. *Mater. Des.* **2016**, *89*, 348–361. [CrossRef]

16. Kitahara, H.; Ueji, R.; Tsuji, N.; Minamino, Y. Crystallographic features of lath martensite in low-carbon steel. *Acta Mater.* **2006**, *54*, 1279–1288. [CrossRef]
17. Lambert-Perlade, A.; Gourgues, A.-F.; Besson, J.; Sturel, T.; Pineau, A. Mechanisms and modeling of cleavage fracture in simulated heat-affected zone microstructures of a high-strength low alloy steel. *Metall. Mater. Trans. A* **2004**, *35*, 1039–1053. [CrossRef]
18. Zhou, W.H.; Guo, H.; Xie, Z.J.; Wang, X.L.; Shang, C.J. High strength low-carbon alloyed steel with good ductility by combining the retained austenite and nano-sized precipitates. *Mater. Sci. Eng. A* **2013**, *587*, 365–371. [CrossRef]
19. Xie, Z.J.; Han, G.; Zhou, W.H.; Zeng, C.Y.; Shang, C.J. Study of retained austenite and nano-scale precipitation and their effects on properties of a low alloyed multi-phase steel by the two-step intercritical treatment. *Mater. Charact.* **2016**, *113*, 60–66. [CrossRef]
20. Wang, X.L.; Wang, X.Y.; Liu, W.L.; Shang, C.J. Effect of Segregation Band on the Microstructure and Properties of a Wind Power Steel before and after Simulated Welding. *Metals* **2024**, *14*, 129. [CrossRef]
21. Luo, H.; Shi, J.; Wang, C.; Cao, W.; Sun, X. Experimental and numerical analysis on formation of stable austenite during the intercritical annealing of 5Mn steel. *Acta Mater.* **2011**, *59*, 4002–4014. [CrossRef]
22. Li, Z.; Chai, F.; Zhang, Z.; Luo, X. Effect of intercritical heat treatment on microstructure, nano-size precipitation and mechanical properties of Fe–Ni–Cu–Al low carbon steel. *Mater. Sci. Eng. A* **2022**, *857*, 144033. [CrossRef]
23. Hosseinifar, F.; Ekrami, A. The effect of cold-rolling prior to the inter-critical heat treatment on microstructure and mechanical properties of 4340 steel with ferrite–martensite microstructures. *Mater. Sci. Eng. A* **2022**, *830*, 142314. [CrossRef]
24. Xie, Z.J.; Shang, C.J.; Subramanian, S.; Ma, X.; Misra, R. Atom probe tomography and numerical study of austenite stabilization in a low carbon low alloy steel processed by two-step intercritical heat treatment. *Scr. Mater.* **2017**, *137*, 36–40. [CrossRef]
25. Fan, H.; Shi, G.; Peng, T.; Wang, Q.; Wang, L.; Wang, Q.; Zhang, F. N-induced microstructure refinement and toughness improvement in the coarse grain heat-affected zone of a low carbon Mo–V–Ti–B steel subjected to a high heat input welding thermal cycle. *Mater. Sci. Eng. A* **2021**, *824*, 141799. [CrossRef]
26. Zhang, X.F.; Han, P.; Terasaki, H.; Sato, M.; Komizo, Y. Analytical investigation of prior austenite grain size dependence of low temperature toughness in steel weld metal. *J. Mater. Sci. Technol.* **2012**, *28*, 241–248. [CrossRef]
27. Zhang, J.; Xin, W.; Ge, Z.; Luo, G.; Peng, J. Effect of high heat input welding on the microstructures, precipitates and mechanical properties in the simulated coarse grained heat affected zone of a low carbon Nb-V-Ti-N microalloyed steel. *Mater. Charact.* **2023**, *199*, 112849. [CrossRef]
28. Yang, Y.; Jia, X.; Ma, Y.; Wang, P.; Zhu, F.; Yang, H. Effect of Nb on microstructure and mechanical properties between base metal and high heat input coarse-grain HAZ in a Ti-deoxidized low carbon high strength steel. *J. Mater. Res. Technol.* **2022**, *18*, 2399–2412. [CrossRef]
29. Qi, X.; Huan, P.; Wang, X.; Liu, Z.; Shen, X.; Gao, Y. Effect of root welding heat input on microstructure evolution and fracture mechanism in intercritically reheat-coarse grained heat-affected zone of X80 pipeline steel. *Mater. Today Commun.* **2022**, *31*, 103413. [CrossRef]
30. Zhang, X.; Miyamoto, G.; Toji, Y.; Zhang, Y.; Furuhara, T. Role of cementite and retained austenite on austenite reversion from martensite and bainite in Fe-2Mn-1.5 Si-0.3 C alloy. *Acta Mater.* **2021**, *209*, 116772. [CrossRef]
31. Hara, T.; Maruyama, N.; Shinohara, Y.; Asahi, H.; Shigesato, G.; Sugiyama, M. Abnormal α to γ Transformation Behavior of Steels with a Martensite and Bainite Microstructure at a Slow Reheating Rate. *ISIJ Int.* **2009**, *49*, 1792–1800. [CrossRef]
32. Nehrenberg, A. Growth of austenite in cold-rolled tempered martensite. *JOM* **1952**, *4*, 181. [CrossRef]
33. Kimmins, S.; Gooch, D. Austenite memory effect in 1 Cr–1 Mo–0· 75V (Ti, B) steel. *Met. Sci.* **1983**, *17*, 519–532. [CrossRef]
34. Nakada, N.; Tsuchiyama, T.; Takaki, S.; Miyano, N. Temperature dependence of austenite nucleation behavior from lath martensite. *ISIJ Int.* **2011**, *51*, 299–304. [CrossRef]
35. Plichta, M.; Aaronson, H. Influence of alloying elements upon the morphology of austenite formed from martensite in Fe-CX alloys. *Metall. Mater. Trans. B* **1974**, *5*, 2611–2613. [CrossRef]
36. Liu, Z.-Q.; Miyamoto, G.; Yang, Z.-G.; Zhang, C.; Furuhara, T. Effects of pre-tempering on intercritical annealing in Fe-2Mn-0.3 C Alloy. *Metall. Mater. Trans. A* **2014**, *45*, 5290–5294. [CrossRef]
37. Zhang, X.; Miyamoto, G.; Toji, Y.; Furuhara, T. Effects of heating rate on formation of globular and acicular austenite during reversion from martensite. *Metals* **2019**, *9*, 266. [CrossRef]
38. Kvackaj, T.; Mamuzic, I. A quantitative characterization of austenite microstructure after deformation in nonrecrystallization region and its influence on ferrite microstructure after transformation. *ISIJ Int.* **1998**, *38*, 1270–1276. [CrossRef]
39. Lan, L.; Qiu, C.; Zhao, D.; Gao, X.; Du, L. Effect of austenite grain size on isothermal bainite transformation in low carbon microalloyed steel. *Mater. Sci. Technol.* **2011**, *27*, 1657–1663. [CrossRef]
40. Babu, N.K.; Suresh, M.; Sinha, P.; Sarma, D. Effect of austenitizing temperature and cooling rate on the structure and properties of a ultrahigh strength low alloy steel. *J. Mater. Sci.* **2006**, *41*, 2971–2980. [CrossRef]
41. Gourgues, A.-F.; Flower, H.; Lindley, T. Electron backscattering diffraction study of acicular ferrite, bainite, and martensite steel microstructures. *Mater. Sci. Technol.* **2000**, *16*, 26–40. [CrossRef]
42. Sun, X.J.; Shang, C.J.; Miao, P.F.; Dong, L.L. Effect of austenitizing temperature on microstructure and properties of low carbon and low crack sensitivity offshore steel. *Trans. Mater. Heat Treat.* **2020**, *41*, 50–56.
43. Furuhara, T.; Kawata, H.; Morito, S.; Miyamoto, G.; Maki, T. Variant selection in grain boundary nucleation of upper bainite. *Metall. Mater. Trans. A* **2008**, *39*, 1003–1013. [CrossRef]

44. Ghosh, A.; Kundu, S.; Chakrabarti, D. Effect of crystallographic texture on the cleavage fracture mechanism and effective grain size of ferritic steel. *Scr. Mater.* **2014**, *81*, 8–11. [CrossRef]
45. Chakrabarti, D.; Strangwood, M.; Davis, C. Effect of bimodal grain size distribution on scatter in toughness. *Metall. Mater. Trans. A* **2009**, *40*, 780–795. [CrossRef]
46. Chhajed, B.; Mishra, K.; Singh, K.; Singh, A. Effect of prior austenite grain size on the tensile properties and fracture toughness of nano-structured bainite. *Mater. Charact.* **2022**, *192*, 112214. [CrossRef]